

# AutoLUT: LUT-Based Image Super-Resolution with Automatic Sampling and Adaptive Residual Learning

Yuheng Xu\* Shijie Yang\* Xin Liu Jie Liu✉ Jie Tang Gangshan Wu

State Key Laboratory for Novel Software Technology, Nanjing University, Nanjing 210023, China

superkenvery@gmail.com {sjyang, xinliu2023}@smail.nju.edu.cn {liujie, tangjie, gswu}@nju.edu.cn

## Abstract

In recent years, the increasing popularity of Hi-DPI screens has driven a rising demand for high-resolution images. However, the limited computational power of edge devices poses a challenge in deploying complex super-resolution neural networks, highlighting the need for efficient methods. While prior works have made significant progress, they have not fully exploited pixel-level information. Moreover, their reliance on fixed sampling patterns limits both accuracy and the ability to capture fine details in low-resolution images. To address these challenges, we introduce two plug-and-play modules designed to capture and leverage pixel information effectively in Look-Up Table (LUT) based super-resolution networks. Our method introduces Automatic Sampling (AutoSample), a flexible LUT sampling approach where sampling weights are automatically learned during training to adapt to pixel variations and expand the receptive field without added inference cost. We also incorporate Adaptive Residual Learning (AdaRL) to enhance inter-layer connections, enabling detailed information flow and improving the network's ability to reconstruct fine details. Our method achieves significant performance improvements on both MuLUT and SPF-LUT while maintaining similar storage sizes. Specifically, for MuLUT, we achieve a PSNR improvement of approximately +0.20 dB improvement on average across five datasets. For SPF-LUT, with more than a 50% reduction in storage space and about a 2/3 reduction in inference time, our method still maintains performance comparable to the original. Code is available at <https://github.com/SuperKenVery/AutoLUT>.

## 1. Introduction

Image Super-Resolution (SR) is the process of enhancing the resolution of an image by reconstructing a High-Resolution (HR) version from Low-Resolution (LR) inputs.

\*: These authors contributed equally to this work.

✉: Corresponding author (liujie@nju.edu.cn).

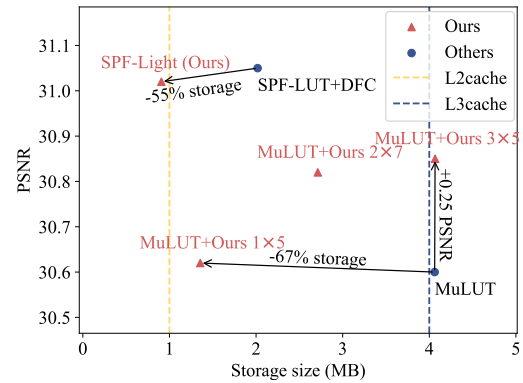


Figure 1. Performance-storage trade-offs for  $\times 4$  super-resolution on Set5 [4] compared with MuLUT [19] and SPF-LUT+DFC [20]. As shown, our method can achieve the same level of performance at much lower storage requirement or much better performance with the same storage.

SR methods based on Deep Neural Networks (DNNs) have demonstrated remarkable success [8, 10, 18, 21, 31, 41, 42], but these deep learning techniques often entail substantial computational demands, making them difficult to deploy.

A significant contribution to addressing these challenges is the SR-LUT [16], which leverages Look-Up Tables (LUTs) to expedite neural network inference. SR-LUT trains a convolutional SR network, then caches its results into an LUT, looks them up during inference, thus reducing computational burden. However, a major limitation of this method is that the size of LUT grows exponentially with the number of input pixels, which limits the receptive field and degrades performance. To overcome this limitation, the subsequent MuLUT [19] uses multiple LUTs, each processing four input pixels sampled from different locations within the image, forming a  $3 \times 3$  receptive field. MuLUT further integrates different strategies within a single LUT group, where each group initially has a receptive field of  $3 \times 3$ . By incorporating a rotation ensemble strategy, this receptive field is expanded to  $5 \times 5$ . Additionally, MuLUT introduces a two-stage SR network that consists of two

LUT groups, resulting in a final receptive field of  $9 \times 9$ . To achieve better performance, SPF-LUT [20] further enlarges the network scale and then proposes a diagonal-first compression technique that preserves the most important parts of the LUT while compressing less important parts more aggressively. This reduces LUT size by approximately 90%. However, SPF-LUT expands the receptive field by deepening the network rather than altering the sampling strategy, it retains the manually designed sampling patterns used by MuLUT, which may not align well with the natural variations in data, limiting the model’s ability to capture fine details accurately. Additionally, previous models did not incorporate residual layers, as adding skip connections would push the LUT values beyond their valid range, making it difficult to preserve their integrity. This lack of residual layers further restricts the flow of information between layers, limiting the model’s ability to learn complex features.

To address these issues, we propose two novel plug-and-play modules for LUT-based SR networks: Automatic Sampling (AutoSample) and Adaptive Residual Learning (AdaRL). AutoSample automatically learns how to sample during training, transforming static pixel extractions into learnable pixel abstractions. This approach allows the receptive field to automatically adapt based on the input during training, providing greater flexibility. AdaRL introduces a modified residual layer that enhances the fusion of information between network layers, improving the flow of detailed information without exceeding the storage constraints of LUTs. Experiments show that our method achieves better performance without additional consumption. As shown in Fig. 1, with more than a 50% reduction in storage space and a 2/3 reduction in inference time, our method still maintains comparable performance. Furthermore, its plug-and-play design allows for easy integration into various networks, providing a performance boost across the entire family of LUT-based SR networks.

The contributions of this work are as follows:

- 1) We propose Automatic Sampling (AutoSample), enabling learnable pixel abstractions that allow for a larger receptive field.
- 2) We introduce the AdaRL layer, adapting the residual technique to LUT-based super-resolution networks to improve the flow of information between layers and enhance model performance.
- 3) We design both the AutoSample and AdaRL layer as plug-and-play modules, enabling flexible integration into LUT-based networks.
- 4) Quantitative and qualitative results demonstrate that our method achieves improved performance while significantly reducing storage space and inference time, making it highly suitable for deployment on resource-limited devices.

## 2. Related Works

**Classical SR Methods.** Classical super-resolution algorithms, such as nearest interpolation, bilinear interpolation, and bicubic interpolation [17], are widely used in emulators and monitors due to their low computational cost, making them suitable for resource-constrained environments. However, they often produce visible artifacts like blurring and aliasing, especially compared to modern DNN-based methods. Additionally, there are exemplar-based methods [11, 12, 25, 34, 35] and sparse-coding methods [26, 28, 29, 37, 38]. While sparse-coding methods can perform well, they are computationally intensive. Other techniques, such as gradient field sharpening [27] and displacement fields[30], also show promise but face challenges with image clarity and high computational requirements.

**DNN Based SR Methods.** With the development of deep learning, many DNN based image super-resolution algorithms have achieved significant restoration performance [2, 6, 7, 9, 14, 18, 21, 31–33, 36, 40, 41]. Early models like SRCNN [9], introduced simple yet effective architectures. The development of residual networks (ResNets) [13] enabled the training of deeper networks by alleviating gradient issues, leading to improvements in SR tasks. EDSR [21] and ESRGAN [31] applied these techniques, achieving state-of-the-art performance by incorporating residual learning and GANs for more realistic outputs. More recently, diffusion-based models [14] have introduced promising generative capabilities to SR. However, while DNN-based methods demonstrate strong restoration abilities, they require significant computational resources due to their complex architectures with large parameter counts.

**Look-Up Table Based SR Methods.** Recently, the use of Look-Up Tables (LUTs) has garnered increasing attention in the field of image restoration due to their low computational cost during inference. SR-LUT [16] pioneered LUT-based image super-resolution, laying the groundwork for this approach. Building upon this foundation, SPLUT [22] improved performance by splitting images into Most Dignificant Bits (MSB) and Least Significant Bits (LSB) and processing each part separately before recombining. MuLUT [19] further extended the receptive field by utilizing multiple LUTs, complementing different sampling methods to achieve a larger receptive field and higher complexity. Most recently, SPF-LUT [20] introduced a diagonal-first compression technique that reduces redundancy by leveraging the commonality of neighboring pixels. However, since SPF-LUT uses the same fixed sampling strategy as MuLUT, the receptive field of a single LUT group remains confined to  $3 \times 3$ , limiting the flexibility for further improvements in feature aggregation.

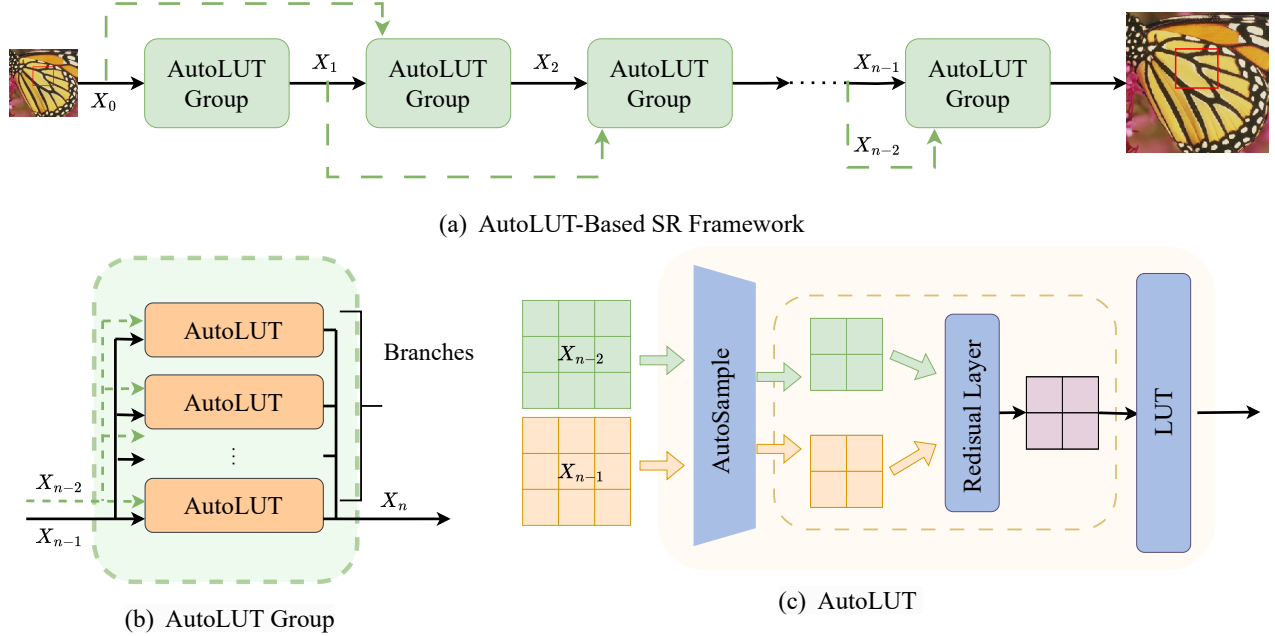


Figure 2. Overview of the AutoLUT-based SR framework. The figure illustrates the process of enhancing LUT-based super-resolution models by integrating the AutoLUT. (a) The AutoLUT-based SR framework replaces traditional LUT Group with AutoLUT Group for improved flexibility. (b) The AutoLUT Group can flexibly adjust the number of branches according to the requirements, enabling more efficient processing of diverse information. (c) The AutoLUT, where the inputs  $X_{n-1}$  and  $X_{n-2}$  pass through the AutoSample, followed by a combination using learnable residual weights. The final output is processed through the basic LUT.

### 3. Method

#### 3.1. Overview

To enhance the performance of LUT-based super-resolution models, several architectural improvements have been proposed. SR-LUT [16] uses a single LUT for mapping inputs to outputs. MuLUT [19] extends this by using two LUT groups, each with three different sampling strategies, forming multiple branches to enhance the model’s flexibility. SPF-LUT [20] takes this a step further by incorporating even more LUT groups, expanding the model’s depth and increasing its capacity to handle complex tasks.

Building upon these advancements, we propose the AutoLUT-based SR framework, a novel architecture that replaces traditional LUT Group with the proposed AutoLUT Group. As shown in Fig. 2, the input to the  $n^{\text{th}}$  group consists of  $X_{n-1}$  and  $X_{n-2}$ , facilitating better communication of fine-grained information across different layers. Previous methods rely on a manually designed, fixed three-branch configuration per LUT group, with each branch selecting four fixed pixels to cover a  $3 \times 3$  receptive field, requiring exactly three branches for full coverage. This hand-crafted approach can not adjust to data variations. In contrast, our AutoLUT automatically learns the optimal sampling strategy directly from the network, allowing a single branch to

cover a  $k \times k$  receptive field and enabling flexible adjustment of branch numbers based on requirements. Specifically, we pass  $X_{n-1}$  and  $X_{n-2}$  through the AutoSample layer, which extracts feature information across the entire receptive field, adapting as needed to achieve full coverage. These are then combined using the AdaRL, and the final output is processed through the basic LUT. This approach enables AutoLUT to create adaptable, learnable representations of pixel values, adjusting branch configurations based on input requirements.

#### 3.2. Automatic Sampling (AutoSample)

As shown in Fig. 3(a), a LUT is a data structure composed of index-value pairs, where sampled indices are used to retrieve their corresponding values. The sampling strategy, which determines how indices are selected, plays a crucial role in mapping them effectively to their values. This directly influences the quality of feature extraction by controlling which information is captured from the input data.

Current methods typically select four fixed pixels directly from the original input, mapping these pixels to their corresponding values, which limits flexibility in handling diverse input. As shown in Fig. 3(b), MuLUT [19] and SPF-LUT [20] employ three distinct sampling strategies, each of which selects four specific pixels from a  $3 \times 3$  input window.

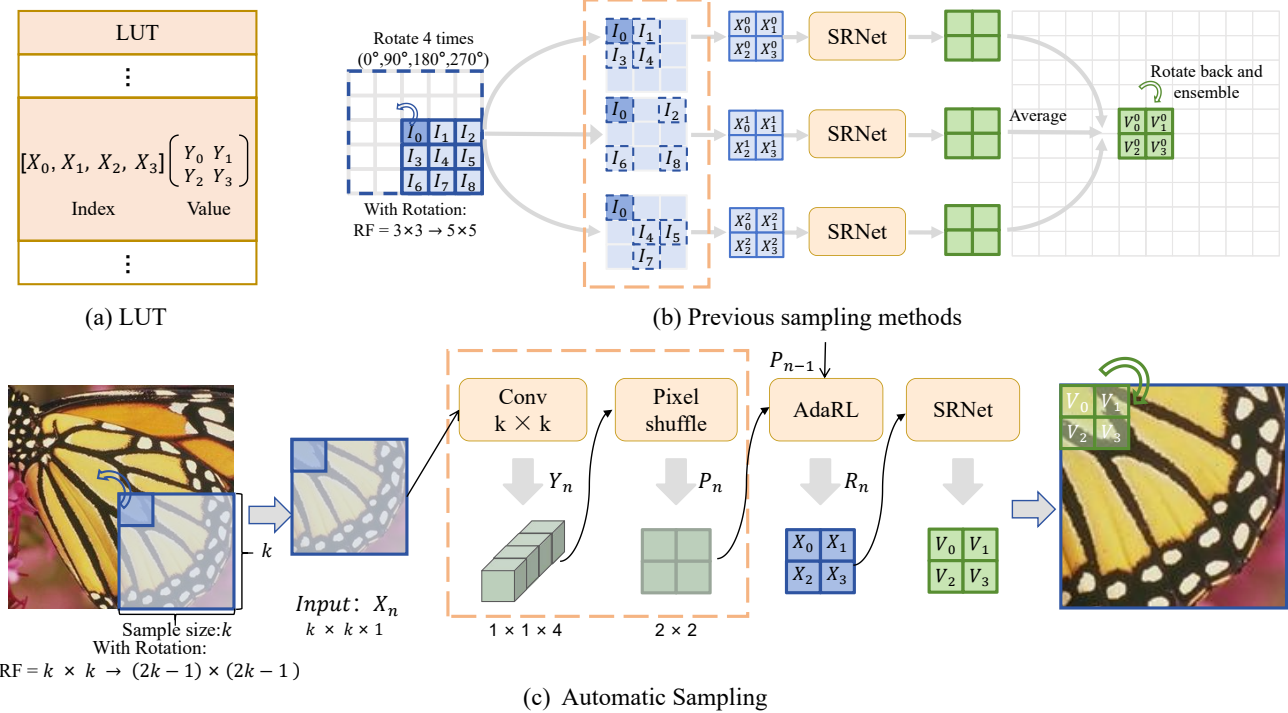


Figure 3. Comparison of sampling strategies on  $\times 2$  super-resolution. (a) A LUT is a data structure composed of index-value pairs, the sampled indices are used to retrieve their corresponding values. (b) The sampling methods in MuLUT [19] and SPF-LUT [20], use three distinct sampling strategies, each selecting four fixed pixels from a  $3 \times 3$  input window. Together, these three sampling configurations fully cover the  $3 \times 3$  window. After applying a rotation ensemble, where the results from four rotated versions are averaged, the receptive field expands from  $3 \times 3$  to  $5 \times 5$ . The pixel  $I_0$  in the low-resolution image corresponds to pixel  $[V_0^0, V_0^1, V_0^2, V_0^3]$  in the image after super-resolution. (c) The learnable AutoSample strategy selects pixels by learning sampling weights through convolution during training, using pixel shuffle to expand the receptive field to  $(2k - 1) \times (2k - 1)$ . Finally, the desired index is obtained by applying AdaRL.

These three sampling configurations collectively cover the entire  $3 \times 3$  region, and with the application of a rotation ensemble [16], the network effectively expands its receptive field from  $3 \times 3$  to  $5 \times 5$ . However, because these strategies are predefined and fixed, they lack the flexibility to adapt to diverse image content or feature distributions. This rigidity restricts the models from adjusting their receptive fields based on specific input characteristics, which may lead to suboptimal performance.

To address these limitations, our approach introduces a learnable sampling strategy, where the network automatically learns how to sample from the input during training. The specific structure is shown in Fig. 3(c). In our framework, we define the sample size as  $k$ , and the input  $X_n$  with dimensions  $k \times k \times 1$  undergoes a convolution operation:

$$Y_n = \text{Conv}(X_n, W), \quad (1)$$

where  $Y_n \in \mathbb{R}^{1 \times 1 \times 4}$ . In the training process, the sampling weights  $W$  with a shape of  $k \times k \times 1 \times 4$  are learned, enabling each output channel in  $Y_n$  to represent a weighted combination of the  $k \times k$  spatial region of the input  $X_n$ .

Specifically, for each output channel  $c$ , the value is computed as a weighted sum of the corresponding input pixels:

$$Y_n^{(c)} = \sum_{i=1}^k \sum_{j=1}^k X_n^{(i,j)} \cdot W^{(i,j,1,c)}. \quad (2)$$

To ensure that the weighted sum does not exceed the range of  $[0, 255]$ , we apply a softmax operation across the  $k \times k$  spatial dimensions of  $W$  before the convolution:

$$W^{(i,j,1,c)} = \frac{\exp(W^{(i,j,1,c)})}{\sum_{i'=1}^k \sum_{j'=1}^k \exp(W^{(i',j',1,c)})}. \quad (3)$$

This normalization is performed over the spatial dimensions  $(0, 1)$ , which ensures that the weights for each output channel in  $W$  are non-negative and sum to one, ensuring that the convolution results stay within  $[0, 255]$ .

To justify the effectiveness of our method, we first introduce convex combination theory [3] as follows:

**Theorem 1.** Given  $n$  values  $a_1, a_2, \dots, a_n$  such that each  $a_i$  lies within an interval  $[a, b]$ , and corresponding

non-negative weights  $\lambda_1, \lambda_2, \dots, \lambda_n$  that sum to 1 (i.e.,  $\sum_{i=1}^n \lambda_i = 1, \lambda_i \geq 0$ ), the weighted sum of these values is:  $\tilde{a} = \sum_{i=1}^n \lambda_i a_i$ . It will also lie within the interval  $[a, b]$ , i.e.,

$$\min(a_1, a_2, \dots, a_n) \leq \tilde{a} \leq \max(a_1, a_2, \dots, a_n).$$

Based on this, our method ensures that the weighted combination of input pixels remains within the  $[0, 255]$ .

Following the convolution, the  $Y_n$  output undergoes a pixel shuffle operation to produce a  $2 \times 2$  grid of pixels, represented as  $P_n$ :

$$P_n = \text{Pixelshuffle}(Y_n). \quad (4)$$

where  $P_n \in \mathbb{R}^{2 \times 2}$ . This operation upscales  $Y_n$  by a factor of 2, redistributing the four output channels in  $Y_n$  to form a  $2 \times 2$  spatial arrangement in  $P_n$ . Each of the four pixels in  $P_n$  is thus a weighted combination of the  $k^2$  surrounding pixels from the original input. At this point, the receptive field is  $k \times k$ , the effective receptive field size expands to  $(2k - 1) \times (2k - 1)$  after a rotation ensemble strategy [16].

By replacing the fixed sampling patterns with AutoSample, our approach provides greater flexibility in both the network’s architecture and its configuration. Unlike previous methods that rely on three distinct, fixed sampling strategies to cover the entire receptive field, our method can use a single AutoSample branch to achieve this. Moreover, our approach allows for the flexible adjustment of the sample size, which directly influences the receptive field. This flexibility not only simplifies the sampling process but also enables the network to automatically learn the sampling strategy. By adding more branches, the network can learn more sampling methods, enhancing its ability to capture diverse features from different input scenarios.

### 3.3. Adaptive Residual Learning (AdaRL)

In LUT-based networks, directly using residual connections may cause the combination of two values within the  $[0, 255]$  range to exceed the LUT’s input range, leading to a dramatic increase in the LUT size. While normalizing the residuals or directly clamping them can prevent the LUT from becoming too large, it results in a loss of precision, which may negatively impact performance [21].

To address this, we propose Adaptive Residual Learning (AdaRL), which performs a weighted average between the current and previous pixel values, maintaining values within a manageable range and preventing the LUT from expanding excessively. AdaRL learns spatially varying weights for each pixel, denoted as  $W_{Residual}$  with a shape  $2 \times 2$ , which determine the contribution of the current and previous pixel values. The weights are clamped between 0 and 1 to ensure a valid range. As shown in Fig. 2(c), the inputs  $X_{n-1}$  and  $X_{n-2}$  undergo the AutoSample process, which extracts

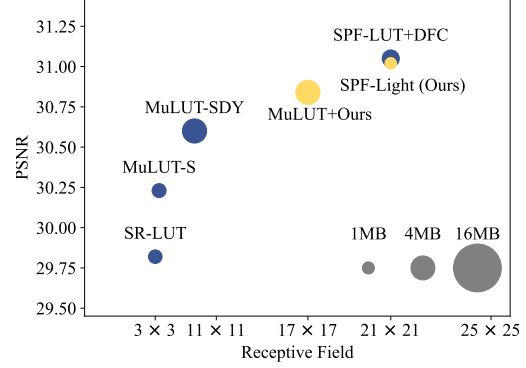


Figure 4. Receptive field and storage comparisons of LUTs. The size of the bubble represents the storage size.

relevant pixel information from the input patch:

$$P_{n-2} = \text{AutoSample}(X_{n-2}), \quad (5)$$

$$P_{n-1} = \text{AutoSample}(X_{n-1}). \quad (6)$$

Then, the sampled outputs  $P_{n-1}$  and  $P_{n-2}$ , each of size  $2 \times 2$ , are combined using the learnable residual weights  $W_{Residual}$  as follows:

$$R_{n-1}^{(i,j)} = (1 - W_{Residual}^{(i,j)}) \odot P_{n-1}^{(i,j)} + W_{Residual}^{(i,j)} \odot P_{n-2}^{(i,j)}, \quad (7)$$

which can be viewed as a convex combination.

According to the Theorem 1,  $P_{n-1}$  and  $P_{n-2}$  are constrained within the range  $[0, 255]$ , and  $W_{Residual} \in [0, 1]$ , the output  $R_{n-1}$  will lie within the range:

$$R_{n-1} \in [\min(P_{n-1}, P_{n-2}), \max(P_{n-1}, P_{n-2})], \quad (8)$$

ensuring that  $R_{n-1}$  remains within the range  $[0, 255]$ .

This confirms that AdaRL preserves precise residual features without causing any issues with LUT size. Therefore, the adaptive weighting in AdaRL ensures that the output  $R_{n-1}$  stays within the desired range of  $[0, 255]$ , maintaining the quality of the image reconstruction and preventing LUT size expansion.

## 4. Experiments and Results

### 4.1. Experiment settings

**Training Settings.** We trained our models on DIV2K [1] dataset and we do evaluation on Set5 [4], Set14 [39], BSDS100 [23], Urban100 [15] and Manga109 [24]. For training, we used the Adam optimizer, chosen for its adaptive learning rate capabilities. The weight decay was set to 0, and the learning rate was initialized at  $10^{-3}$ . We randomly crop images to  $48 \times 48$  patches with a batch size of 32. After training, the models were exported as Look-Up Tables (LUTs). Where necessary, DFC [20] compression was applied to reduce the LUT size. Following this,

Table 1. Quantitative comparison of PSNR/SSIM and storage size on standard benchmark datasets for  $\times 4$  super-resolution. We applied AutoSample and AdaRL to SPF-LUT [20] and MuLUT [19]. Using our method on MuLUT with 3 branches and sample size 5, we achieved better performance while maintaining nearly the same storage size. On SPF-LUT, our method achieved comparable performance with less than half the storage. The gray background highlights our methods. For MuLUT and SPF-LUT, the best results are in **bold**.

	Method	Storage Size	Set5 [4]	Set14 [39]	BSDS100 [23]	Urban100 [15]	Manga109 [24]
Classical	Nearest	-	26.25/0.7372	24.65/0.6529	25.03/0.6293	22.17/0.6154	23.45/0.7414
	Zeyde et al. [38]	-	26.69/0.8429	26.90/0.7354	26.53/0.6968	23.90/0.6962	26.24/0.8241
	Bilinear	-	27.55/0.7884	25.42/0.6792	25.54/0.6460	22.69/0.6346	24.21/0.7666
	Bicubic	-	28.42/0.8101	26.00/0.7023	25.96/0.6672	23.14/0.6574	24.91/0.7871
	NE + LLE [5]	1.434MB	29.62/0.8404	26.82/0.7346	26.49/0.6970	23.84/0.6942	26.10/0.8195
	ANR [28]	1.434MB	29.70/0.8422	26.86/0.7386	26.52/0.6992	23.89/0.6964	26.18/0.8214
	A+ [29]	15.17MB	30.27/0.8602	27.30/0.7498	26.73/0.7088	24.33/0.7189	26.91/0.8480
MuLUT	MuLUT [19]	4.062MB	30.60/0.8653	27.60/0.7541	26.86/0.7110	24.46/0.7194	27.90/0.8633
	MuLUT+DFC [20]	<b>0.407MB</b>	30.55/0.8642	27.56/0.7532	26.83/0.7104	24.41/0.7177	27.82/0.8613
	MuLUT+ours	4.067M	<b>30.85/0.8699</b>	<b>27.77/0.7584</b>	<b>26.96/0.7144</b>	<b>24.60/0.7257</b>	<b>28.27/0.8706</b>
SPF-LUT	SPF-LUT [20]	17.284MB	<b>31.11/0.8764</b>	<b>27.92/0.7640</b>	<b>27.10/0.7197</b>	<b>24.87/0.7378</b>	<b>28.68/0.8796</b>
	SPF-LUT+DFC [20]	2.018MB	31.05/0.8755	27.88/0.7632	27.08/0.7190	24.81/0.7357	28.58/0.8779
	SPF-Light	<b>0.907MB</b>	31.02/0.8751	27.88/0.7629	27.07/0.7186	24.78/0.7342	28.54/0.8769
DNN	RRDB [31]	63.942MB	32.68/0.8999	28.88/0.7891	27.82/0.7444	27.02/0.8146	31.57/0.9185
	EDSR [21]	164.396MB	32.46/0.8968	28.80/0.7876	27.71/0.7420	26.64/0.8033	31.02/0.9148
	RCAN [41]	59.74MB	32.61/0.8999	28.93/0.7894	27.80/0.7436	26.85/0.8089	31.45/0.9187
	SwinIR [42]	170.4MB	32.44/0.8976	28.77/0.7858	27.69/0.7406	26.47/0.7980	30.92/0.9151

a LUT-aware fine-tuning phase was performed [19], during which the LUT contents were treated as trainable parameters, allowing for further optimization of the network’s performance. During fine-tuning, the AutoSample and AdaRL were fine-tuned together.

To verify the effectiveness of our modules, we apply them to MuLUT [19] and SPF-LUT [20]. Specifically, we conduct experiments with different parameter combinations, including the number of branches and the sample size  $k$ . In our setup, “MuLUT+Ours  $b \times k$ ” denotes the specific configuration with the number of branches  $b$  and sample size  $k$ . Throughout the following sections, MuLUT+Ours specifically implies the configuration with 3 branches and sample size 5. Additionally, we implement a lightweight version of SPF-LUT, called SPF-Light, by replacing and reducing the number of branches in each group to one. This adjustment is intended to significantly reduce storage space requirements, allowing us to explore the efficiency of our method in optimizing model size without compromising performance.

**Comparison Models and Metrics.** We evaluate our approach against a variety of super-resolution methods, including interpolation-based techniques (nearest neighbor, bilinear, bicubic interpolation), sparse coding methods (NE+LLE [5], ANR [28] and A+ [29]) and DNN methods (RRDB [41], EDSR [21], RCAN [41], SwinIR [42]). We additionally compare with MuLUT [19] and SPF-LUT [20]. We test Peak Signal-to-Noise Ratio (PSNR) and Structural Similarity Index Measure (SSIM) for quantitative evaluation.

tion.

## 4.2. Experimental Results and Analysis

**Quantitative Comparison.** We evaluate our framework on five datasets, using PSNR and SSIM as metrics. As shown in Table. 1, when our proposed modules are integrated into MuLUT, we observe a +0.20 dB improvement in PSNR on average across the datasets. Specifically, on the Set5 dataset, the PSNR increases by 0.25 dB, on the Manga109 dataset, the PSNR improves by 0.37 dB. These results clearly demonstrate that our method provides substantial performance improvements, with a negligible increase in storage size (from 4.062 MB to 4.067 MB). We conducted a further visual analysis in Fig. 1 and Fig. 4. As shown, SPF-Light reduces storage by 55% while maintaining performance comparable to SPF-LUT+DFC (Fig. 1), with the same receptive field (Fig. 4). Additionally, MuLUT+Ours greatly expands the receptive field without increasing storage, resulting in a 0.25 dB PSNR improvement on Set5. Moreover, MuLUT+Ours  $1 \times 5$  reduces storage by about 67% compared to MuLUT while exceeding its PSNR performance. Our method maintains the performance while significantly reducing storage, offering a more efficient solution for LUT-based super-resolution networks.

**Qualitative Comparison.** As shown in Fig. 5, MuLUT+Ours produces clearer results, particularly on images of butterfly and the letter ‘e’, where MuLUT often displays severe artifacts. In comparison with SPF-LUT+DFC, our SPF-Light achieves similar performance, while requiring

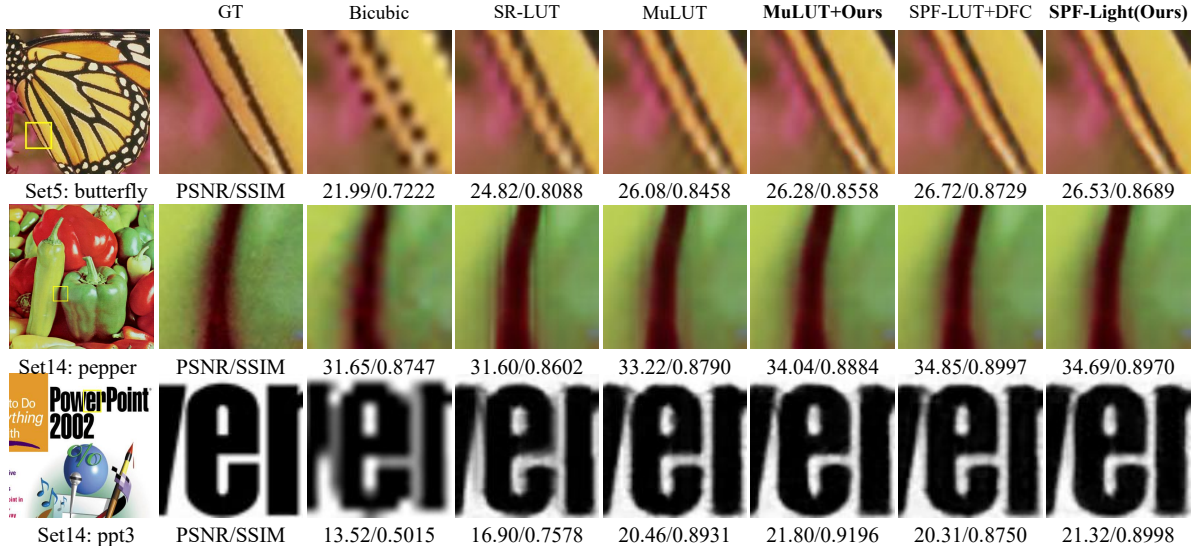


Figure 5. Qualitative comparison for  $\times 4$  super-resolution on benchmark datasets. Our methods are in **bold**.

Table 2. Ablation study on different branch numbers and sample sizes for  $\times 4$  super-resolution on MuLUT.

Configuration				PSNR/SSIM				
	Branches	Sample Size	Storage Size	Set5	Set14	BSDS100	Urban100	Manga109
①	2	3	2.710MB	30.73/0.8677	27.68/0.7566	26.92/0.7130	24.54/0.7233	28.14/0.8680
②		3	4.065MB	30.79/0.8693	27.72/0.7579	26.94/0.7142	24.57/0.7249	28.20/0.8696
③	3	5	4.067MB	30.85/0.8699	27.77/0.7584	26.96/0.7144	24.60/0.7257	28.27/0.8706
④		7	4.069MB	30.82/0.8694	27.72/0.7578	26.95/0.7146	24.58/0.7247	28.20/0.8693
⑤	4	3	5.424MB	30.83/0.8700	27.73/0.7586	26.96/0.7148	24.60/0.7262	28.26/0.8708

less than half the storage space.

### 4.3. Ablation Study

We conducted ablation experiments across different components and hyperparameters to investigate the impact of factors such as the number of branches, sample size, and the inclusion of AutoSample and AdaRL on performance.

**Sample Size.** We conducted experiments using different sample sizes 3, 5 and 7 with 3 branches, as shown in rows ②, ③, ④ of the Table. 2. The sample size 5 achieved the empirically better results in terms of both PSNR and SSIM across all datasets. Additionally, as the sample size increased, storage requirements only increased marginally 0.002 MB per increment in sample size, demonstrating the method’s efficiency in handling larger receptive fields with negligible additional storage. However, when the sample size increased to 7, performance decreased slightly, with PSNR dropping by 0.03 dB on Set5. This may be due to the excessively large receptive field introducing irrelevant information that did not contribute effectively to the model’s performance.

**Branches.** We conducted experiments using branches 2, 3 and 4 with sample size 3, as shown in rows ①, ②, ⑤ of the

Table. 2. As the number of branches increases, the PSNR progressively improves, reaching 30.73 dB, 30.79 dB and 30.83 dB on Set5. This improvement highlights the effectiveness of increasing the number of branches, which enhances the model’s ability to capture detailed information. However, increasing the number of branches also leads to higher storage requirements. To strike a balance between performance and efficiency, we chose to use 3 branches with sample size 5 for MuLUT, as it provided empirically better performance while keeping storage manageable.

**AutoSample and AdaRL.** The ablation study results in Table. 3, using 3 branches and sample size 3, highlight the individual and combined contributions of the AutoSample and AdaRL. For example, on Set5, adding only the AutoSample module results in a PSNR increase from 30.60 dB to 30.63 dB. Meanwhile, incorporating only the AdaRL module provides a more substantial boost, with PSNR increasing to 30.70 dB. When both modules are applied, performance reaches a PSNR of 30.79 dB. This demonstrates that each module enhances super-resolution independently, and their combination achieves the best results. The same trend is reflected across other datasets, reinforcing the com-

Table 3. Ablation study on AutoSample and AdaRL for  $\times 4$  super-resolution.

	Automatic Sampling	AdaRL	Set5	Set14	BSDS100	Urban100	Manga109
①	-	-	30.60/0.8653	27.60/0.7541	26.86/0.7110	24.46/0.7194	27.90/0.8633
②	✓	-	30.63/0.8657	27.63/0.7550	26.86/0.7112	24.49/0.7204	28.02/0.8627
③	-	✓	30.70/0.8687	27.67/0.7572	26.89/0.7136	24.51/0.7242	28.07/0.8685
④	✓	✓	30.79/0.8693	27.72/0.7579	26.94/0.7142	24.57/0.7249	28.20/0.8696

Table 4. Comparison of runtime and PSNR across different SR methods on Set5 on mobile device.

	Runtime (ms)	PSNR
MuLUT[19]	5938.1	30.60
MuLUT+Ours $1 \times 5$	2043.95	30.62
MuLUT+Ours	5984.00	30.85
SPF-LUT+DFC[20]	31921.65	31.05
SPF-Light (Ours)	9910.95	31.02

plementary strengths of AutoSample and AdaRL.

#### 4.4. Inference Performance on Edge Device

To systematically compare the performance of various super-resolution methods on mobile devices, we converted each model to ONNX format and tested them on an Android smartphone, specifically the OnePlus Ace 3 Pro running ColorOS 14. The super-resolution processing was performed on the Snapdragon 8 Gen 3 CPU’s Cortex-X4 core at 2.4 GHz, and the results were obtained when running  $\times 4$  super-resolution on a  $224 \times 224$  image.

The experimental results are summarized in Table 4. For instance, MuLUT+Ours  $1 \times 5$  with 1 branch and sample size 5, reduces inference time significantly, from 5938.10 ms to 2043.95 ms, while also increasing PSNR by 0.02 dB compared to MuLUT. Similarly, SPF-Light reduces inference time from 31921.65 ms to 9910.95 ms, with a negligible PSNR decrease upon SPF-LUT+DFC. Notably, MuLUT+Ours achieves nearly the same inference time as MuLUT while increasing PSNR by 0.25 dB. Overall, our method achieves inference time reductions of about two-thirds on both MuLUT and SPF-LUT, with performance comparable to or even exceeding the original models. These results are also visually represented in Fig. 6, our model demonstrates both lower inference time and improved performance. Our methods, represented in red, consistently occupy the Pareto optimal region in the upper-left quadrant, highlighting their advantage in achieving high efficiency while maintaining excellent performance.

### 5. Conclusion

We propose two novel plug-and-play modules, AutoSample and AdaRL, to improve the performance of LUT-

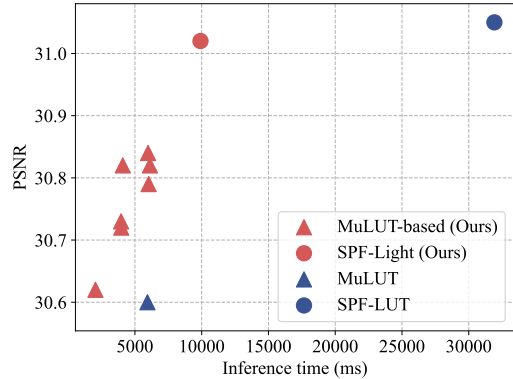


Figure 6. Comparison of inference time and performance of different SR methods. Top-left is better. Red denotes networks with our methods, and Blue means other methods. Our methods consistently occupy the Pareto optimal region in the upper-left quadrant, highlighting their advantage in achieving high efficiency while maintaining excellent performance.

based super-resolution networks. AutoSample dynamically adapts the pixel extraction process by learning sampling weights during training, enabling it to expand the receptive field without increasing storage requirements and capture more detailed information. Meanwhile, AdaRL enhances the flow of information between layers through residual learning. Together, these modules enable significant reductions in storage space and inference time, making our approach particularly well-suited for deployment on resource-limited edge devices. The modular architecture of AutoSample and AdaRL allows for easy integration into a variety of LUT-based super-resolution networks, enabling efficient deployment of super-resolution models. Through experiments, we demonstrate the advantages of our method in terms of reduced storage size, improved performance, and faster runtime on resource-limited edge devices.

### Acknowledgments

This work was supported by the National Natural Science Foundation of China (Grant No. 62402211) and the Natural Science Foundation of Jiangsu Province (Grant No. BK20241248). The authors would also like to thank the support from the Collaborative Innovation Center of Novel Software Technology and Industrialization, Jiangsu, China.

## References

- [1] Eirikur Agustsson and Radu Timofte. Ntire 2017 challenge on single image super-resolution: Dataset and study. In *The IEEE Conference on Computer Vision and Pattern Recognition (CVPR) Workshops*, 2017. 5
- [2] Namhyuk Ahn, Byungkon Kang, and Kyung-Ah Sohn. Fast, accurate, and lightweight super-resolution with cascading residual network. In *ECCV*, 2018. 2
- [3] Dimitri Bertsekas, Angelia Nedic, and Asuman Ozdaglar. *Convex analysis and optimization*. Athena Scientific, 2003. 4
- [4] Marco Bevilacqua, Aline Roumy, Christine Guillemot, and Marie-Line Alberi-Morel. Low-complexity single-image super-resolution based on nonnegative neighbor embedding. In *BMVC*, 2012. 1, 5, 6
- [5] Hong Chang, Dit-Yan Yeung, and Yimin Xiong. Super-resolution through neighbor embedding. In *CVPR*, 2004. 6
- [6] Chang Chen, Zhiwei Xiong, Xinmei Tian, Zheng-Jun Zha, and Feng Wu. Camera lens super-resolution. In *CVPR*, 2019. 2
- [7] Zhen Cheng, Zhiwei Xiong, Chang Chen, Dong Liu, and Zheng-Jun Zha. Light field super-resolution with zero-shot learning. In *CVPR*, 2021. 2
- [8] Chao Dong, Chen Change Loy, Kaiming He, and Xiaoou Tang. Learning a deep convolutional network for image super-resolution. In *ECCV*, 2014. 1
- [9] Chao Dong, Chen Change Loy, Kaiming He, and Xiaoou Tang. Image super-resolution using deep convolutional networks. *IEEE Trans. Pattern Anal. Mach. Intell.*, 38(2):295–307, 2016. 2
- [10] Chao Dong, Chen Change Loy, and Xiaoou Tang. Accelerating the super-resolution convolutional neural network. In *ECCV*, 2016. 1
- [11] William T. Freeman, Egon C. Pasztor, and Owen T. Carmichael. Learning low-level vision. *Int. J. Comput. Vis.*, 40(1):25–47, 2000. 2
- [12] William T. Freeman, Thouis R. Jones, and Egon C. Pasztor. Example-based super-resolution. *IEEE Computer Graphics and Applications*, 22(2):56–65, 2002. 2
- [13] Kaiming He, Xiangyu Zhang, Shaoqing Ren, and Jian Sun. Deep residual learning for image recognition. In *2016 IEEE Conference on Computer Vision and Pattern Recognition, CVPR 2016, Las Vegas, NV, USA, June 27-30, 2016*, pages 770–778. IEEE Computer Society, 2016. 2
- [14] Jonathan Ho, Ajay Jain, and Pieter Abbeel. Denoising diffusion probabilistic models. In *Advances in Neural Information Processing Systems 33: Annual Conference on Neural Information Processing Systems 2020, NeurIPS 2020, December 6-12, 2020, virtual*, 2020. 2
- [15] Jia-Bin Huang, Abhishek Singh, and Narendra Ahuja. Single image super-resolution from transformed self-exemplars. In *CVPR*, 2015. 5, 6
- [16] Younghyun Jo and Seon Joo Kim. Practical single-image super-resolution using look-up table. In *CVPR*, 2021. 1, 2, 3, 4, 5
- [17] R. Keys. Cubic convolution interpolation for digital image processing. *IEEE Transactions on Acoustics, Speech, and Signal Processing*, 29:1153–1160, 1981. 2
- [18] Jiwon Kim, Jung Kwon Lee, and Kyoung Mu Lee. Accurate image super-resolution using very deep convolutional networks. In *CVPR*, 2016. 1, 2
- [19] Jiacheng Li, Chang Chen, Zhen Cheng, and Zhiwei Xiong. MuLUT: Cooperating multiple look-up tables for efficient image super-resolution. In *ECCV*, 2022. 1, 2, 3, 4, 6, 8
- [20] Yinglong Li, Jiacheng Li, and Zhiwei Xiong. Look-up table compression for efficient image restoration. In *Proceedings of the IEEE/CVF Conference on Computer Vision and Pattern Recognition (CVPR)*, pages 26016–26025, 2024. 1, 2, 3, 4, 5, 6, 8
- [21] Bee Lim, Sanghyun Son, Heewon Kim, Seungjun Nah, and Kyoung Mu Lee. Enhanced deep residual networks for single image super-resolution. In *CVPRW*, 2017. 1, 2, 5, 6
- [22] Cheng Ma, Jingyi Zhang, Jie Zhou, and Jiwen Lu. Learning series-parallel lookup tables for efficient image super-resolution. In *Computer Vision - ECCV 2022 - 17th European Conference, Tel Aviv, Israel, October 23-27, 2022, Proceedings, Part XVII*, pages 305–321. Springer, 2022. 2
- [23] David R. Martin, Charless C. Fowlkes, Doron Tal, and Jitendra Malik. A database of human segmented natural images and its application to evaluating segmentation algorithms and measuring ecological statistics. In *ICCV*, 2001. 5, 6
- [24] Yusuke Matsui, Kota Ito, Yuji Aramaki, Azuma Fujimoto, Toru Ogawa, Toshihiko Yamasaki, and Kiyoharu Aizawa. Sketch-based manga retrieval using manga109 dataset. *Multim. Tools Appl.*, 76(20):21811–21838, 2017. 5, 6
- [25] Guoping Qiu. Interresolution look-up table for improved spatial magnification of image. *J. Vis. Commun. Image Represent.*, 11(4):360–373, 2000. 2
- [26] Yaniv Romano, John Isidoro, and Peyman Milanfar. RAISR: rapid and accurate image super resolution. *IEEE Trans. Computational Imaging*, 3(1):110–125, 2017. 2
- [27] Qiang Song, Ruiqin Xiong, Dong Liu, Zhiwei Xiong, Feng Wu, and Wen Gao. Fast image super-resolution via local adaptive gradient field sharpening transform. *IEEE TIP*, 27(4):1966–1980, 2018. 2
- [28] Radu Timofte, Vincent De Smet, and Luc Van Gool. Anchored neighborhood regression for fast example-based super-resolution. In *ICCV*, 2013. 2, 6
- [29] Radu Timofte, Vincent De Smet, and Luc Van Gool. A+: adjusted anchored neighborhood regression for fast super-resolution. In *ACCV*, 2014. 2, 6
- [30] LingFeng Wang, Huai-Yu Wu, and Chunhong Pan. Fast image upsampling via the displacement field. *IEEE TIP*, 23(12):5123–5135, 2014. 2
- [31] Xintao Wang, Ke Yu, Shixiang Wu, Jinjin Gu, Yihao Liu, Chao Dong, Yu Qiao, and Chen Change Loy. ESRGAN: enhanced super-resolution generative adversarial networks. In *ECCV Workshops*, 2018. 1, 2, 6
- [32] Zeyu Xiao, Zhiwei Xiong, Xueyang Fu, Dong Liu, and Zheng-Jun Zha. Space-time video super-resolution using temporal profiles. In *ACM MM*, 2020.

- [33] Zeyu Xiao, Xueyang Fu, Jie Huang, Zhen Cheng, and Zhiwei Xiong. Space-time distillation for video super-resolution. In *CVPR*, 2021. [2](#)
- [34] Zhiwei Xiong, Xiaoyan Sun, and Feng Wu. Robust web image/video super-resolution. *IEEE TIP*, 19(8):2017–2028, 2010. [2](#)
- [35] Zhiwei Xiong, Dong Xu, Xiaoyan Sun, and Feng Wu. Example-based super-resolution with soft information and decision. *IEEE Trans. Multim.*, 15(6):1458–1465, 2013. [2](#)
- [36] Ruikang Xu, Zeyu Xiao, Mingde Yao, Yueyi Zhang, and Zhiwei Xiong. Stereo video super-resolution via exploiting view-temporal correlations. In *ACM MM*, 2021. [2](#)
- [37] Jianchao Yang, John Wright, Thomas S. Huang, and Yi Ma. Image super-resolution via sparse representation. *IEEE TIP*, 19(11):2861–2873, 2010. [2](#)
- [38] Roman Zeyde, Michael Elad, and Matan Protter. On single image scale-up using sparse-representations. In *Curves and Surfaces*, 2010. [2](#), [6](#)
- [39] Roman Zeyde, Michael Elad, and Matan Protter. On single image scale-up using sparse-representations. In *International conference on curves and surfaces*, pages 711–730. Springer, 2010. [5](#), [6](#)
- [40] Haochen Zhang, Dong Liu, and Zhiwei Xiong. Two-stream action recognition-oriented video super-resolution. In *ICCV*, 2019. [2](#)
- [41] Yulun Zhang, Kunpeng Li, Kai Li, Lichen Wang, Bineng Zhong, and Yun Fu. Image super-resolution using very deep residual channel attention networks. In *ECCV*, 2018. [1](#), [2](#), [6](#)
- [42] Yulun Zhang, Yapeng Tian, Yu Kong, Bineng Zhong, and Yun Fu. Residual dense network for image super-resolution. In *CVPR*, 2018. [1](#), [6](#)